INTERFACE SCIENCE 12, 303–310, 2004

Atomic Scale Chemistry of α_2/γ Interfaces in a Multi-Component TiAl Alloy

STEPHAN S.A. GERSTL
Department of Materials Science and Engineering, Northwestern University, Evanston, IL 60208, USA

YOUNG-WON KIM
UES, Dayton, OH 45432, USA

DAVID N. SEIDMAN
Department of Materials Science and Engineering, Northwestern University, Evanston, IL 60208, USA

Abstract. We report on the distribution of micro-alloying elements in a multi-component TiAl-based alloy. The specimen contains 3 at.% Nb, 1.5 at.% Cr, 0.5 at.% Mn, 0.6 at.% (W + Hf + Zr), and 0.2 at.% each of B, C, and O. The distributions of all micro-alloying elements with respect to the heterophase interface between α_2 and γ lamellae are analyzed with a three-dimensional atom-probe (3DAP) microscope. All the elements partition except boron, which resides primarily in boride precipitates. Oxygen, C, Mn, and Cr partition to the α_2-phase, whereas Nb and Zr partition to the γ-phase. Both W and Hf exhibit excess concentration values within ca. 7 nm of the lamellar interface in the α_2-phase, and their near interfacial excesses are 0.26 and 0.35 atoms nm^{-2}, respectively.

Keywords: TiAl, interface, partitioning, proxigram, interfacial excess

1. Introduction

Titanium aluminide intermetallics are promising materials for high-temperature structural applications primarily due to their inherently low density, as well as their good oxidation and creep resistance, and high strength [1, 2]. Fine lamellar microstructures composed of alternating α_2 and γ lamellae, 10–30 nm thick, are known to improve high-temperature creep resistance [3]. Micro-alloying elements are introduced to form strengthening precipitates, refine the lamellar spacings, and improve creep and oxidation resistance [4–6]. The detailed distribution of the alloying elements, however, is poorly characterized. In this article, we present analyses of the partitioning of all components among the intermetallic phases in a prototype-engineering alloy.

2. Experimental Procedures

The alloy employed was produced by induction skull melting and hot isostatic pressing and has a composition of Ti-46.5 Al-1.5 Cr-0.5 Mn-3 Nb-0.2 W-0.2 Hf-0.2 Zr-0.2 B-0.2 C-0.2 O (at.%). It was forged isothermally at 1423 K to 91% reduction. The oxygen content is introduced by these processing techniques. The alloy was annealed at 1553 K, then aged at 1073 K for 24 hr, and finally cooled in air to room temperature.

Transmission electron microscopy (TEM) specimens were prepared utilizing an electrolytic solution of 10 vol.% perchloric acid in methanol at -25°C in a Struers Tenupol 5 dual-jet electropolisher. Three dimensional atom-probe (3DAP) microscopy specimen blanks were prepared using electro-discharge machining to dimensions of 213 μm $\times$ 213 μm $\times$ 15 mm.

Specimens for 3DAP microscopy were prepared by electropolishing, initially in a solution of 5 vol.% perchloric in glacial acidic acid, followed by a solution of 2 vol.% perchloric in butoxyethanol, to form apexes with a radius of ca. 50 nm.

Conventional and high-resolution TEM was performed on the Hitachi 8100 and HF-2000 microscopes respectively, both operating at 200 kV. To obtain chemical information, we used a 3DAP microscope, which yields an atom-by-atom reconstruction in direct space of a volume of material, typically $20 \times 20 \times 100$ nm^3. Each atom is identified chemically and positioned utilizing a time-of-flight mass spectrometer and a two-dimensional position–sensitive detector. Such analyses allow local chemical gradients near an interface to be quantified on the sub- to nanometer length scale. The 3DAP microscope investigations were performed using a 19% pulse fraction, at 60 K, and a pulse frequency of 1.5 kHz. A custom software program, *ADAM* 1.5 [7, 8], developed at Northwestern University, was used for analyzing the 3DAP microscopy data.

The mass spectrum contains a few mass-to-charge state (m/n) peak overlaps due to the multi-component nature for the alloy; for example, the following pairs of peaks overlap: $^{180}Hf^{2+}$– $^{90}Zr^{1+}$, $^{182}W^{2+}$– $^{91}Zr^{1+}$, $^{184}W^{2+}$– $^{92}Zr^{1+}$, and $^{186}W^{2+}$– $^{93}Nb^{1+}$. A mass spectrum with some peak overlaps is exhibited in Fig. 1. Peaks representing more than one ion type (making up less than 0.3% of the data) are omitted from the reconstructed data to avoid ambiguity.

3. Experimental Investigations

3.1. Microstructural Characterization: Transmission Electron Microscopy

The alloy microstructure, displayed in a low magnification micrograph in Fig. 2, consists primarily of α_2-Ti_3Al and γ-TiAl phases with hexagonal $D0_{19}$ and tetragonal $L1_0$ structures, respectively. This figure exhibits a duplex microstructure with both single-phase γ and lamellar α_2-γ grains. Within the lamellar grains, the alternating α_2 and γ lamellae exhibit a wide range of thicknesses. The α_2-Ti_3Al lamellae are 5 to 50 nm wide, whereas the γ-TiAl lamellae are 10 to 150 nm wide. The lamellar thicknesses vary significantly among the lamellar colonies. The lamellae within individual lamellar colonies, however, vary in thickness by only ±30%. The individual colonies make up 26% of the microstructure; the remainder of the microstructure is a combination of single-phase γ-grains and boride and carbide precipitates.

The interface structure between α_2 and γ lamellae was investigated utilizing high-resolution electron microscopy (HREM). The lamellar interfaces were observed by orienting the plane of the interface parallel to the electron beam. Figure 3 is a typical lamellar interface revealing an atomically sharp boundary between the α_2 and γ lamellae. There was no observable transition region between the lamellae and few interfaces revealed misfit dislocations. The orientation

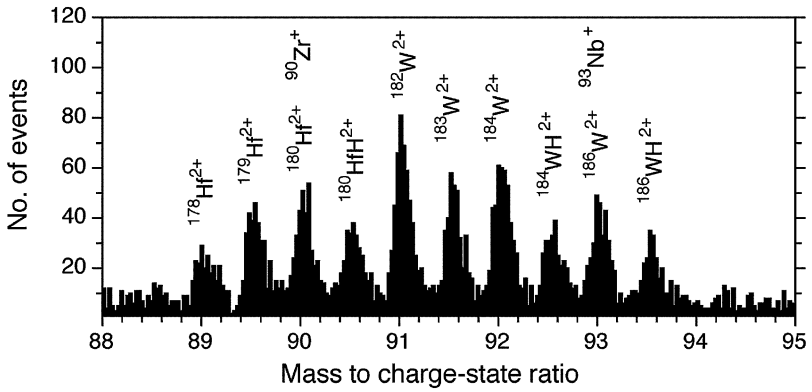

Figure 1. Mass spectrum demonstrating instrumental mass resolution and possible peak overlaps. The overlapping peaks (making up <0.3% of all data) were not included in data analyses to guarantee uniqueness of elemental concentrations. Zr primarily field-evaporates in the doubly charged state ($^{90}Zr^{++}$), therefore little or no overlap with other Zr isotopes occurs in the mass range 91–94 amu.

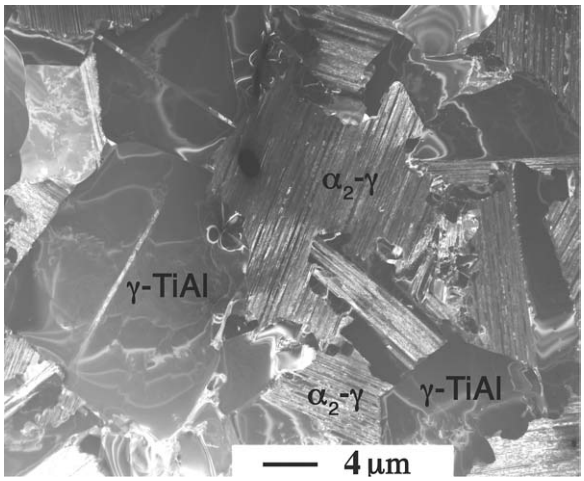

Figure 2. Bright field TEM micrograph of the duplex microstructure of the titanium aluminide alloy, having both single-phase γ and lamellar α_2/γ grains.

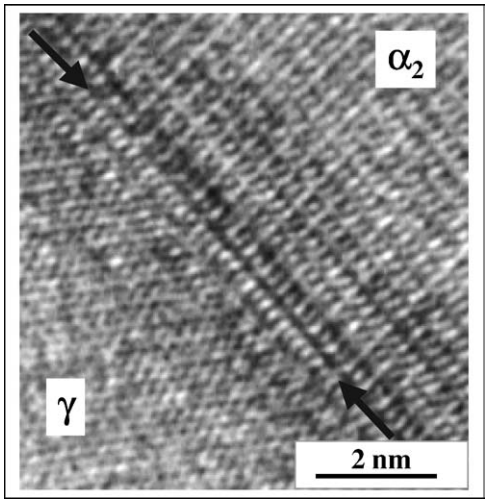

Figure 3. High-resolution electron microscope (HREM) micrograph displaying a typical atomically sharp interface between lamellae. No misfit dislocations are identified in this micrograph.

relationship is

$$(111)_\gamma \parallel (0001)_{\alpha_2} \quad \text{and} \quad \langle 1\bar{1}0\rangle_\gamma \parallel \langle 11\bar{2}0\rangle_{\alpha_2}$$

which is in agreement with the results of Blackburn [9]. Now we discuss the distribution of micro-alloying elements within such microstructures, particularly near the lamellar interfaces.

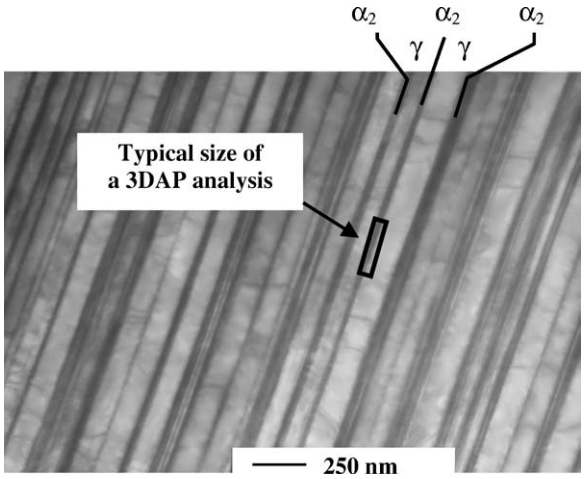

Figure 4. Bright-field TEM micrograph comparing the α_2/γ lamellar structure to a 3DAP microscope analysis cross-sectional area. The superimposed 3DAP microscope analysis area shows that the lamellar interface is parallel to the 3DAP microscope analysis direction.

3.2. *Chemical Analysis: Three-Dimensional Atom-Probe Microscopy*

3DAP microscope analyses of two α_2/γ lamellar interfaces were carried out (referred to as Nos. 1 and 2). Figure 4 demonstrates the typical size of a 3DAP analysis superimposed on a TEM micrograph of the lamellar microstructure. Figure 5 exhibits the 3D reconstruction of the α_2/γ lamellar interface representing interface No. 1 (see on-line version of this paper for a colored figure). The interface, represented as a green surface, is identified by an isoconcentration surface defined by a 55 at.% Ti concentration threshold [7, 8]. Concentrations of all identified elements are then measured at subnanometer distances from either side of the interface and plotted in the form of a proximity histogram (or proxigram for short) [7].

Figures 6 and 7 exhibit the proxigrams for interface Nos. 1 and 2, respectively. The proxigrams display the constituent compositions in the vicinity of the interface. The concentrations of the partitioning micro-alloying elements are presented in Table 1. The micro-alloying additions Cr, Mn, C, and O partition to the α_2-phase, whereas Nb and Zr preferentially reside in the γ-phase. Tungsten and hafnium, however, exhibit no significant partitioning; instead they exhibit strikingly similar near interfacial excesses in proximity to the α_2/γ interface in the α_2-phase (noted by arrows in Fig. 7 and detailed in Fig. 8). In interface No. 1, the concentrations of W and Hf are distinctly higher in the α_2-phase within 0–4 nm of the interface. A similar behavior is observed

Table 1. Concentrations (at.%) of all elements, except B, W and Hf, summarizing two 3DAP analyses of α_2/γ lamellar interfaces. Concentrations of partitioning micro-alloying elements are in bold font. Boron is not displayed as it primarily resides in boride precipitates, while W and Hf do not partition to either phase, but exhibit near interfacial excesses on the α_2 side of the interface. The uncertainties represent plus or minus one sigma.

	α_2	γ	Partitioning ratios (α_2:γ)
Ti	59.2 ± 0.42	49.94 ± 1.53	1.2:1
Al	32.41 ± 0.42	43.93 ± 2.09	1:1.4
O	$\mathbf{1.12 \pm 0.11}$	0.08 ± 0.06	13.9:1
C	$\mathbf{0.61 \pm 0.08}$	0.15 ± 0.05	4.0:1
Cr	$\mathbf{2.61 \pm 0.16}$	1.76 ± 0.86	1.5:1
Mn	$\mathbf{0.81 \pm 0.09}$	0.63 ± 0.10	1.3:1
Zr	0.21 ± 0.04	$\mathbf{0.28 \pm 0.09}$	1:1.4
Nb	2.56 ± 0.12	$\mathbf{3.13 \pm 0.71}$	1:1.2

within 2–7 nm of interface No. 2. The near interfacial excesses of W and Hf are 0.26 and 0.35 atoms nm^{-2}, respectively, calculated from the shaded regions displayed in Fig. 8. The calculations involve multiplying the shaded region (concentrations times the bin size of 1 nm) by the theoretical density of the α_2-phase, since the concentrations are measured in that phase.

4. Discussion

4.1. Microstructural Characterization

Lamellar thicknesses are known to vary with cooling rate [7]. As this alloy was air cooled, the wide range of lamellar thicknesses discussed above is attributed to the nucleation and growth of lamellar colonies at different times during the final air-cooling procedure. Chromium influences the lattice parameters in both intermetallic phases [10], thus affecting the misfit between them. In the present alloy, there are many interstitial (B, C, O) and substitutional (Nb, Cr, Mn, Zr) elements that can affect the lattice constants, consequently also decreasing the misfit between the two phases. HREM observations reveal atomically sharp interfaces (Fig. 3) supporting these conjectures. Although most of the interfaces observed are atomically sharp we observed periodic dislocations and growth ledges along 10% of the lamellar interfaces. The addition of B to TiAl alloys has been theoretically [5] and experimentally [11] investigated and has been shown to refine grain sizes and lamellar thicknesses. Carbon additions primarily form carbide precipitates, which increase the creep resistance [5]. This paper presents its interstitial behavior in either intermetallic phase.

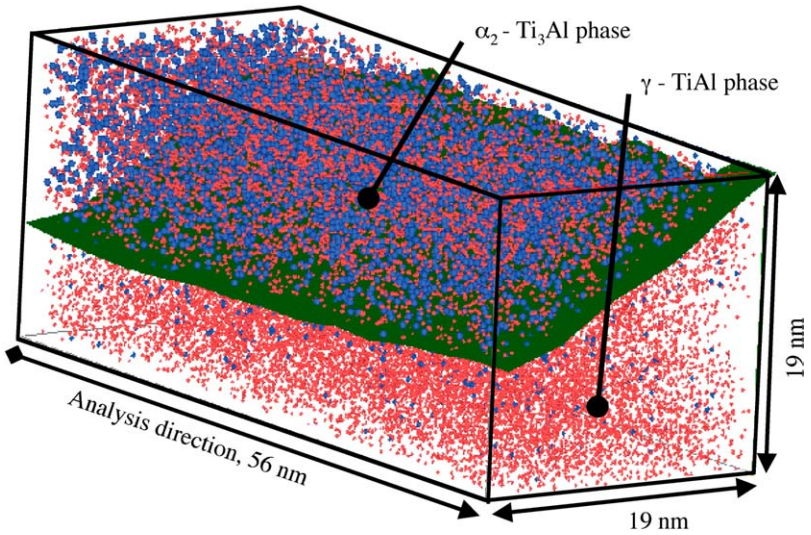

Figure 5. A 3DAP microscopy reconstruction of an α_2/γ interface parallel to the analysis direction. The 55 at.% Ti isoconcentration surface (in green) defines the interface between the two phases. Nb (red) and O (blue) are displayed to show their different partitioning behaviors. Other elements are not displayed for the sake of clarity. Colors refer to the on-line version of this paper.

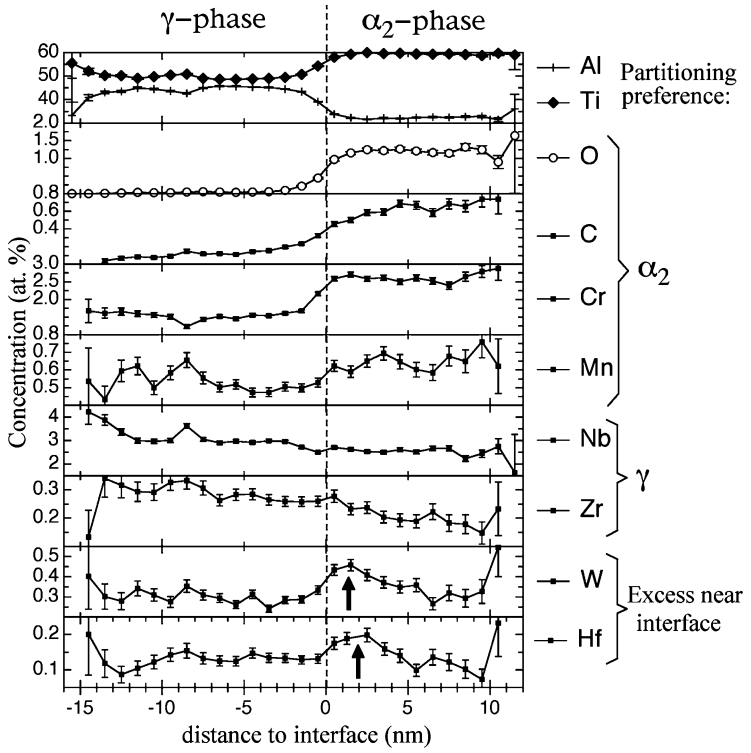

Figure 6. Proximity histogram of the 3DAP microscopy analysis of interface No. 1, revealing partitioning behaviors of all elements. Boron resides primarily in the form of boride particles and hence is not displayed. Each elemental concentration is displayed on its own ordinate axis in at.%. The γ-phase is on the left-hand side and the α_2-phase is displayed on the right-hand side.

4.2. Chemical Analysis: Three-Dimensional Atom-Probe Microscope Investigation

Partitioning behaviors of the micro-alloying elements are in agreement with previous studies of similar alloys using atom-probe microscopy techniques [12–14], with the exception of W and Hf, which do not exhibit significant partitioning to either phase. Spatially resolved concentration measurements of W and Hf near the lamellar interface reveal a local enhancement within 7 nm of the lamellar interface in the α_2-phase. It has been suggested that tungsten stabilizes the α_2 lamellae against dissolution during aging of the microstructure [6, 11]. In view of the spatial correlation between W and Hf in two separate analyses, it is suggested that Hf serves a similar strengthening role in TiAl alloys. The formation of the β-phase (B2 structure) adjacent to lamellar interfaces has been observed in other TiAl alloys after creep experiments and is suggested to be part of a decomposition process of the α_2-phase [15, 16]. It is also established that Cr, W, V, and Nb stabilize the β-phase [17, 18]. If what we observed was part of a β-phase precipitate, Cr and Nb would be expected to exhibit concentration gradients similar to those of W and Hf. However, the Cr and Nb concentrations do not show localized excesses such as those displayed by W and Hf.

The random orientation of the lamellar grains in the microstructure can result in 3DAP microscope analyses along a variety of directions with respect to the lamellar interfaces, be it parallel, perpendicular or oblique to the interface. The data presented includes only those analyses that were parallel to a lamellar interface, as represented in Figs. 4 and 5. Analyzing an interface in a parallel orientation results in interfacial areas greater than ca. 1000 nm^2, whereas an analysis of an interface perpendicular to the analysis direction is limited to interfacial areas of ca. 360 nm^2. Due to the seven micro-alloying elements present at low concentrations (<0.6 at.%), a greater analyzed area is necessary to provide more atoms parallel to the interface, thereby resulting in statistically significant data.

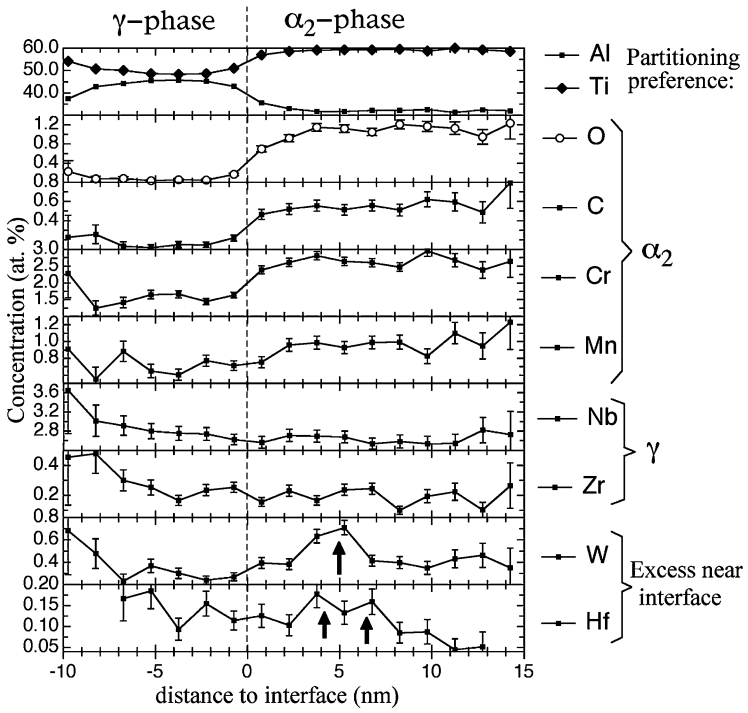

Figure 7. Proximity histogram of 3DAP microscopy analysis of interface No. 2, revealing similar partitioning behaviors of detected elements. Boron resides primarily in the form of boride particles and hence is not displayed.

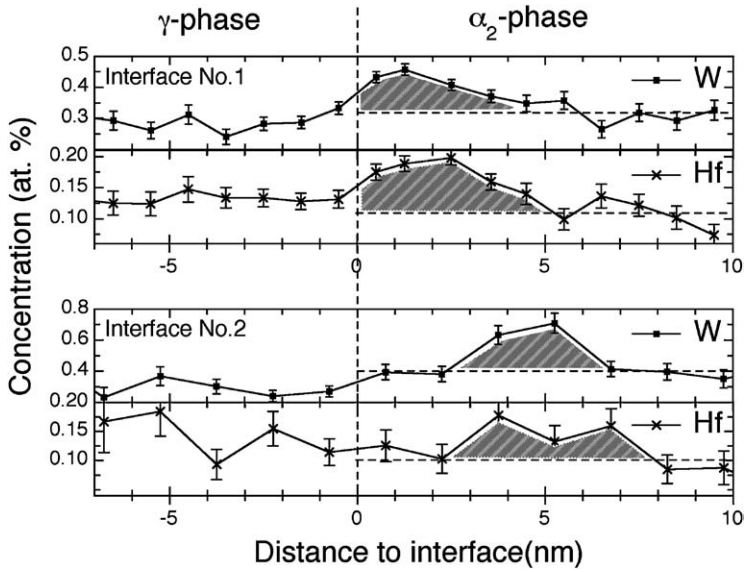

Figure 8. Concentration gradients of W and Hf near both lamellar interfaces, numbered 1 and 2, demonstrate near interfacial excesses (shaded regions) in the α_2-phase of 0.26 and 0.35 atoms nm^{-2}, respectively. The horizontal dotted lines represent concentrations of the elements in the α_2-phase, not including the concentration gradients.

We now comment on interface sharpness as determined by HREM and 3DAP microscopies. For a 3DAP microscope analysis direction parallel to the interface plane, there exists the possibility of field-evaporation trajectory effects [19] because each phase field-evaporates at slightly different values of the local electric field. Therefore, when two phases field-evaporate simultaneously, their different field-evaporation characteristics must be taken into account when interpreting the 3D reconstruction [20]. Since the expected evaporation field of Ti (26 V nm^{-1}) is greater than that for Al (19 V nm^{-1}) [21], the higher Ti-containing phase, α_2, field-evaporates at a higher local electric field than the γ-phase. The specimen voltage was measured to be 3% higher when field-evaporating the α_2-phase compared to field-evaporating the γ-phase. This observed increase in specimen voltage confirms that the α_2-phase field-evaporates at a higher electric field than the γ-phase. For a 3DAP microscope analysis parallel to an α_2/γ interface, the γ-phase field-evaporates preferentially, which affects the accurate composition measurements of the different phases (Table 1). When the ions impinge on the 2D position sensitive detector, the overlapping ion trajectories, due to the 3% difference in field-evaporation conditions, cause the interfacial boundary, represented via the proxigram, to display a wider interface [22] than the one structurally observed by HREM, which demonstrates that the interfaces are atomically sharp (Fig. 3).

4.3. Elemental Partitioning

The partitioning of oxygen was observed to be the most pronounced, as reported elsewhere [12, 23, 24]. Oxygen prefers the α_2-phase to the γ-phase by a ratio of almost 14:1. Our analyses show that the oxygen concentration reaches 0.09 at.% in the γ-phase and 1.24 at.% in the α_2-phase. This is inconsistent, however, with Menand et al.'s suggested maximum oxygen concentration of 0.025 at.% in the γ-phase [24]. Menand et al.'s thorough study of oxygen concentrations in a $Ti_{54}Al_{46}$ alloy suggests that the multi-component nature of our alloy can have a significant effect on the maximum concentration of oxygen dissolved in the γ-phase.

The remaining micro-alloying elements partition according to their positions in the periodic table. The metalloids (C and O) and transition metals (Cr and Mn), periods two and four respectively, partition to the α_2-phase, whereas period five elements (Nb and Zr) partition to the γ-phase. Elements from period six (W and Hf) do not show a preference for either phase and appear to create a concentration gradient in the α_2-phase within 7 nm of the interface. We note that the correlation of partitioning behavior with periodic table period would not necessarily follow for all possible dopants.

It has been suggested that W provides an impurity drag effect on interfaces [6], thereby reducing interface mobility. Tungsten has also been proven to stabilize the α_2-phase from dissolution during aging [11], thus increasing the creep resistance. Our observations indicate a spatial correlation between W and Hf in our alloy due to their striking similarity in near interfacial excesses within 7 nm of the lamellar interfaces.

5. Conclusions

- The partitioning behaviors of O, C, Cr, and Mn to the α_2-phase and Nb and Zr to the γ-phase, are in agreement with published results on γ-based TiAl alloys, with the caveat that the present alloy is a complex multi-component system. The oxygen concentration in the γ-phase of our alloy is more than twice the oxygen concentration detected in the γ-phase of binary TiAl alloys [24], most likely due to the presence of seven additional micro-alloying elements in our alloy.
- The effect of field-evaporation of the two intermetallic phases is discussed. Due to the parallel orientation of the α_2/γ interface to the 3DAP microscope analysis direction, there may be field-evaporation trajectory effects, causing the 3D-reconstruction of the interface to appear somewhat wider than it should be [22]. HREM observations reveal the lamellar interfaces to be atomically sharp, devoid of misfit dislocations.
- Our observation of a tungsten excess of 0.26 atoms nm^{-2} within 7 nm of the α_2/γ interface on the α_2-side, supports the view that W stabilizes the α_2-phase against dissolution during aging and creep. Hafnium shows similar characteristics to W (with an excess of 0.35 atoms nm^{-2}), suggesting it could serve a similar role in stabilizing the α_2/γ lamellar interface during creep.

Acknowledgments

The authors would like to thank Dr. Roy Benedek for helpful discussions and carefully reading the manuscript. This research was supported by the DOE Basic Sciences Division.

References

1. Y.W. Kim, JOM-J. Miner. Met. Mater. Soc. **47**, 39 (1995).
2. F. Appel and R. Wagner, Mat. Sci. Eng. **R22**, 187 (1998).
3. S. Karthikeyan, G.B. Viswanathan, P.I. Gouma, V.K. Vasudevan, Y.W. Kim, and M.J. Mills, Mat. Sci. Eng. A **329**, 621 (2002).
4. S. Kim, G.D.W. Smith, S.G. Roberts, and A. Cerezo, Mat. Sci. Eng. A **250**, 77 (1998).
5. P.K. Khowash, D.L. Price, and B.R. Cooper, Mat. Res. Soc. Symp. Proc. **213**, 31 (1991).
6. D.J. Larson, C.T. Liu, and M.K. Miller, Intermetallics **5**, 497 (1997).
7. O.C. Hellman, J.A. Vandenbroucke, J. Rüsing, D. Isheim, and D.N. Seidman, Microsc. Microanal. **6**, 437 (2000).
8. O.C. Hellman, J. Vandenbroucke, J. Blatz du Rivage, and D.N. Seidman, Mat. Sci. Eng. A **327**, 29 (2002).
9. M.J. Blackburn, in *The Science, Technology and Applications of Titanium*, edited by R.J. a. N.E. Promisel (Pergamon Press, Oxford, England, 1970).
10. W. Wunderlich, T. Kremser, and G. Fommeyer, Acta Metall. **41**, 1791 (1993).
11. R.V. Ramanujan, P.J. Maziasz, and C.T. Liu, Acta Metall. **44**, 2611 (1996).
12. D.J. Larson and M.K. Miller, Mater. Charact. **44**, 159 (2000).
13. S. Kim and G.D.W. Smith, Mat. Sci. Eng. A **240**, 229 (1997).
14. A. Menand, in *Gamma Titanium Aluminides* (The Minerals, Metals, and Materials Society, Warrendale, PA, 1999), p. 111.
15. D.Y. Seo, J. Beddoes, L. Zhau, and G.A. Botton, Mat. Sci. Eng. A **329–331**, 810 (2002).
16. Z.W. Huang, W. Voice, and P. Bowen, Scripta Mater. **48**, 79 (2003).
17. K. Subramanian, Ph.D. Thesis, Ohio State University, 2003.
18. G. Shao and P. Tsakiropoulos, Mat. Sci. Eng. A **329–331**, 914 (2002).
19. F. Vurpillot, A. Bostel, and D. Blavette, Appl. Phys. Lett. **76**, 3127 (2000).
20. W. Lefebvre, A. Menand, A. Loiseau, and D. Blavette, Mat. Sci. Eng. A **327**, 40 (2002).
21. M.K. Miller, A. Cerezo, M.G. Hetherington, and G.D. Smith, *Atom. Probe Field Ion. Microscopy* (Clarendon Press, Oxford, 1996).
22. D. Isheim and D.N. Seidman, Surface and Interface Analysis, 2004, in press.
23. A. Menand, H. Zapolsky-Tatarenko, and A. Nerac-Partaix, Mat. Sci. Eng. A **250**, 55 (1998).
24. A. Menand, A. Huguet, and A. NeracPartaix, Acta Mater **44**, 4729 (1996).